

Entering a New Dimension in Powder Processing for Advanced Ceramics Shaping

Johanna Christiane Sanger,* Brian Richard Pauw, Birte Riechers, Andrea Zocca, Julian Rosalie, Robert Maa, Heinz Sturm, and Jens Gunster*

Filigree structures can be manufactured via two-photon polymerization (2PP) operating in the regime of nonlinear light absorption. For the first time, it is possible to apply this technique to the powder processing of ceramic structures with a feature size in the range of the critical defect sizes responsible for brittle fracture and, thus, affecting fracture toughness of high-performance ceramics. In this way, tailoring of advanced properties can be achieved already in the shaping process. Traditionally, 2PP relies on transparent polymerizable resins, which are diametrically opposed to the usually completely opaque ceramic resins and slurries. Here a transparent and photocurable suspension of nanoparticles (resin) with very high mass fractions of yttria-stabilized zirconia particles (YSZ) is presented. Due to the extremely well-dispersed nanoparticles, scattering of light can be effectively suppressed at the process-relevant wavelength of 800 nm. Sintered ceramic structures with a resolution of down to 500 nm are obtained. Even at reduced densities of 1–4 g cm⁻³, the resulting compressive strength with 4.5 GPa is equivalent or even exceeding bulk monolithic yttria-stabilized zirconia. A ceramic metamaterial is born, where the mechanical properties of yttria-stabilized zirconia are altered by changing geometrical parameters, and gives access to a new class of ceramic materials.

1. Introduction

The success of many natural materials, such as bone, enamel, and nacre, relies on a unique combination between a hierarchical microstructure and optimized topology.^[1–3] The former spans from the atomic level to the size of tens of micrometer large crystallites, and the latter uses specific geometric patterns or arrangements that are adapted to the materials' service conditions. In concert, this synergy gives rise to property combinations that cannot be achieved by classical materials design, where monolithic materials and their microstructure are the focus.^[4]

This realization spawned so-called metamaterials^[5] where materials' scientists seek to mimic nature, thereby creating a new wide spectrum of functional^[6] and mechanical properties,^[7] some of which are unifying the best property combinations know to-date. Examples include mechanical metamaterials with densities of a few percent compared to their bulk counterparts,^[8] but yet with exceptional

strength, and metamaterials for optical cloaking or broadband polarization.^[9,10] Much of this progress was driven by new routes of micro- and nanostructuring additive manufacturing (AM) technologies, continuously pushing the boundaries of both the resolution of periodically arranged ligaments and the processable materials.^[11]

Central to the disruptive AM technology is the ability of immediate complex geometry printing with a material of choice, which bears the promise of reducing large prototyping and small-series manufacturing costs. Being able to directly print an intricate 3D object, AM is the ideal processing route to design and create novel metamaterials, where topological feature sizes and microstructural length-scales now can overlap. A technology that brings this length-scale convergence to the extreme is two-photon polymerization (2PP), where nonlinear light absorption allows printing polymeric metamaterials with feature sizes smaller than 100 nm.^[12] In this process, polymeric prelattices are produced via 3D direct laser writing. The prelatice is subsequently covered with a nm-thick layer of a metal^[13] or ceramic,^[14] and a polymer-based composite metamaterial is obtained. If desired, the polymer prelatice can also be removed, giving, for example, rise to hollow ceramic^[15] structures with remarkable properties.

J. C. Sanger, B. R. Pauw, B. Riechers, A. Zocca, J. Rosalie, R. Maa, H. Sturm, J. Gunster

Federal Institute for Materials Research and Testing (BAM)

Unter den Eichen 87, 12205 Berlin, Germany

E-mail: johanna.saenger@bam.de; jens.guenster@bam.de

R. Maa

Department of Materials Science and Engineering

University of Illinois at Urbana-Champaign

Urbana, IL 61801, USA

H. Sturm

IWF

Technical University Berlin


Pascalstr. 8–9, 10587 Berlin, Germany

J. Gunster

Institute of Non-Metallic Materials

Clausthal University of Technology

38678 Clausthal-Zellerfeld, Germany

 The ORCID identification number(s) for the author(s) of this article can be found under <https://doi.org/10.1002/adma.202208653>.

© 2022 The Authors. Advanced Materials published by Wiley-VCH GmbH. This is an open access article under the terms of the Creative Commons Attribution License, which permits use, distribution and reproduction in any medium, provided the original work is properly cited.

DOI: 10.1002/adma.202208653

Despite these milestones in structural and topological design, a central shortcoming remains the inevitable use of a photocurable polymeric resin and precursor, which hampers direct printing of a metal or ceramic metamaterial. Indeed, printing directly fully metallic or ceramic metamaterials via 2PP seems impossible, being fundamentally limited by the light scattering of the solid phases in a resin that reduces the photon density. A first step in overcoming this limitation has been the development of 2PP-compatible transparent polymer-derived ceramics (PDCs) that yield polymeric parts.^[16] A pyrolysis transforms the resulting structure into glassy inorganic materials.^[17,18] Glass components are formed by inserting silica nanoparticles into PDCs.^[18,19] Coatings can be applied to improve the mechanical properties.^[20] And by combining 2PP and digital light processing (DLP) with the same PDC resin parts with multiscale features can be achieved.^[21] The metamaterial properties of PDCs benefit from reduced strut thickness at the microscale.^[22] While this is promising, metamaterials obtained from preceramic polymers substantially fall behind the thermomechanical and extreme physicochemical properties advanced ceramics are known for.

In the present communication, we demonstrate how to unlock the full potential of technical ceramics in 2PP-designed metamaterials, based on preliminary work.^[23] Reducing the ceramic particle size and narrowing down their size distribution sufficiently, allows for the first-time powder processing with 2PP without detrimental light scattering. Specifically, a transparent ceramic slurry of extremely well-dispersed yttria and zirconia nanoparticles can produce monolithic yttria-stabilized zirconia (YSZ) structures with ligament sizes between 400 and 500 nm. This constitutes the highest resolution of powder-based AM of fully ceramic materials so far, thereby entering a length-scale regime in which ceramic metamaterials can profit from size-dependent strengthening and toughening. Indeed, since the fracture strength, σ_f , of brittle materials is limited by the size of pre-existing flaws,^[24,25] smaller objects are known to be stronger and tougher, approximately following a scaling of $\sigma_f \propto 1/\sqrt{l}$, where l is the limiting physical dimension.^[26] This promotes ultrastrong nanoscale materials that at the bulk scale are weak and brittle. A well-known classical example exploiting this concept is the strengthening of polymeric materials by thin glass fibers, so-called glass fiber reinforced polymers (GFRP).^[27] As such, the here-demonstrated nanoscale 2PP AM process does now allow designing fully ceramic metamaterials and nanostructures, analog to PDC structures,^[28] where size effects and their extreme physicochemical properties, guarantee thermodynamic stability and outstanding mechanical performance even at large surface areas and finest feature sizes.

2. Results and Discussion

We begin with highlighting the ceramic 2PP AM processing by producing a hollow and complex 3D micromodel of a lattice cube structure shown in **Figure 1a**. An excellent in-plane accuracy compared to the computer-aided design CAD model of **Figure 1d** is seen. Due to a co-sintering of substrate and lattice structure, only the first layer of unit cells in direct contact with the substrate shows some distortion. For details on the

processing technique, we refer to the “Experimental Section.” The side view in **Figure 1b** reveals the generally observed reduced z-dimension resolution for 2PP. The quality and resolution of the powder-processed structure is remarkable, given a post 2PP sintering step at 1200 °C that causes considerable co-shrinking. In fact, the initial cube lattice had a side length of 40 μm prior to sintering, that is being reduced by ≈40% to 25 μm. Such a large linear shrinkage is due to the high sintering activity of the nanoscale ceramic particles contained in the transparent feedstock. Already at 800 °C the onset of sintering is observed and structures with high structural stability and strength are formed.

Conventional ceramic stereolithography resins rely on powders with particles typically originating from ball milling that may have a monodispersed particle distribution with a mean size of 0.45–10 μm. Here, we have used particles produced with a hydrothermal process, yielding sizes below 100 nm. Despite this nanoscopic powder, particle agglomeration remains absent, as verified with small-angle X-ray scattering (SAXS). Specifically, the structures displayed in **Figure 1** were printed using yttria-stabilized zirconia powder with a hydrodynamic particle size of 35 nm, as determined by dynamic light scattering (DLS). Additionally, volume-weighted particle size distributions obtained through SAXS show a distribution spanning from ≈1–30 nm (assuming approximately spherical-shaped particles), with a volume-weighted mean diameter of 11.1 nm, as shown in **Figure 2a**. This particle shape assumption and SAXS-derived size distribution are supported by, and in agreement with, transmission electron microscopy bright-field imaging (**Figure 2b**). The smaller particle size from SAXS compared to DLS is expected, as the former measures the actual particle size, where the latter returns a mass-squared-weighted hydrodynamic particle diameter, i.e., including a water shell surrounding the scatterer, whose extent varies depending on the interface chemistry.^[29] In the considered particle size regime, the contribution of the water shell can be significant, as shown in this example, but it is, on the other hand, irrelevant for the scattering of light.

It is this progress in formulating a nanoparticle containing photoactive resin with high optical transmittance and suitable viscosity, shown in **Figures S1 and S2** (Supporting Information), that allows sub-micrometer 2PP AM of ceramic microlattices and structures. An insight into the volume of a hollow printed cube is provided by a cross-sectional cut in **Figure S3** (Supporting Information). The smaller the particle size, the smaller the light scattering, and the higher the transmittance for 2PP. At a ceramic particle weight fraction of 70 wt%, a transmittance of the resin of 95% could be measured at a wavelength of 800 nm and a light path of 100 μm. To underline this high transmittance, the resin containing various particle weight fractions was UV-cured, and its optical transmittance at a wavelengths of 400, 600 and 800 nm was evaluated. **Figure 2c** summarizes the cured resin transmittance.

A curious effect was observed with the concentration series depicted in **Figure 2c**. Initially, with ceramic contents between 0 and 35 wt%, an increase in the number density of ceramic nanoparticles leads to a concomitant reduction in transmittance, down to ≈50% at 35 wt%, with the films gradually assuming a milky off-white appearance. Beyond this low point, however,

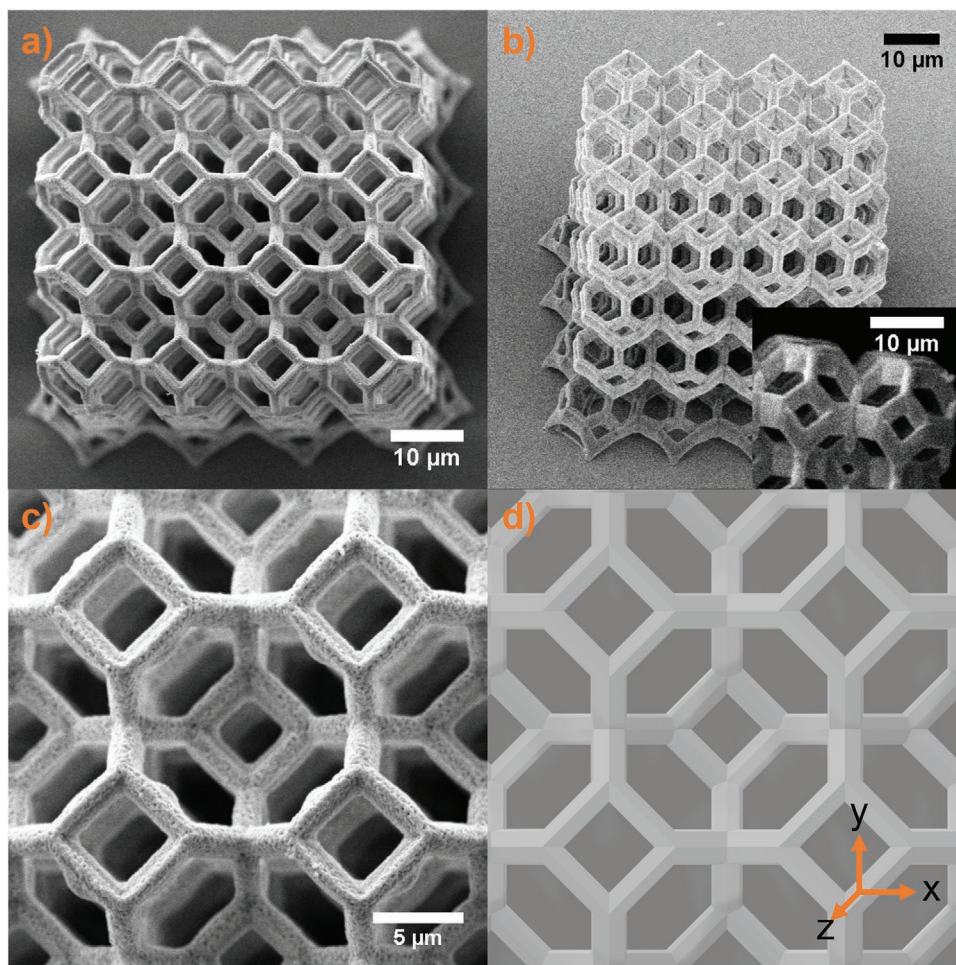


Figure 1. 3D additive manufacturing via two-photon polymerization and sintering at 1200 °C. a) Undistorted lattice cube with an in-plane x-y resolution of 1 μm top view. b) 45° and 90° (inset) side views. c) The zoom-in shows individual ligaments. d) CAD model.

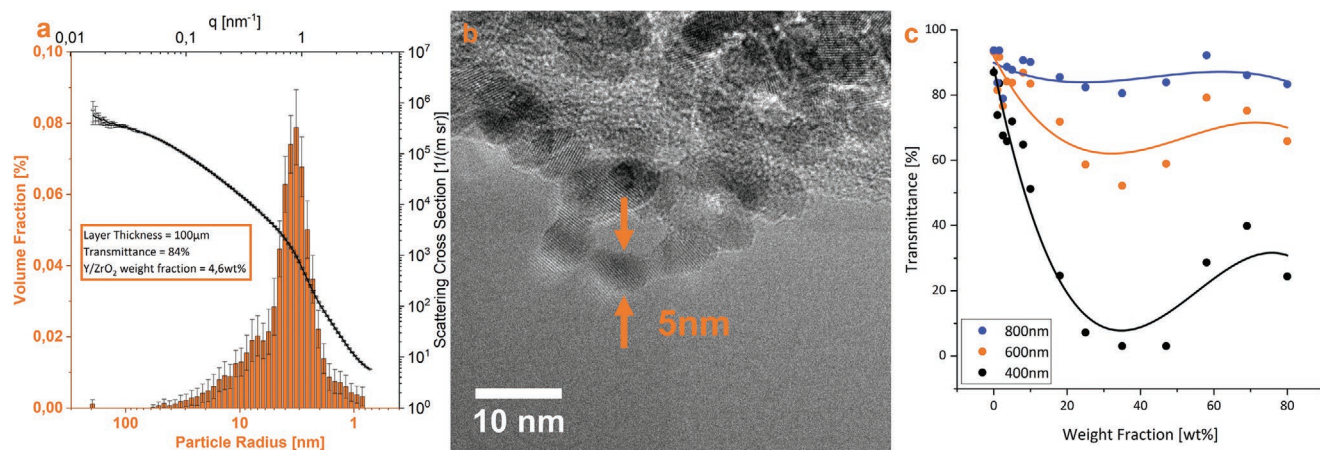


Figure 2. Physical characterization of the ceramic nanoparticles and its 2PP-suitable resin. a) Particle size distribution of yttria-stabilized zirconia from SAXS-measurements of a resin with 4.6 wt% at 100 μm layer thickness and a transmittance of 84%. b) Transmission electron microscopy (TEM) image of single particles. The size of one particle is indicated. c) Transmittance of cured resin with rising yttria-stabilized zirconia weight fraction demonstrating high transmittance across a large weight fraction range and a transmittance anomaly in the intermediate regime, for three wavelengths of the incident light of 400, 600 and 800 nm.

the transmittance gradually increases again, reaching values close to the dilute limit even at 60 wt%. SAXS investigation of the complete series does not show any indications of particle agglomeration or imperfect mixing, yet it does show the expected monotonically increasing interparticle interference effects due to their increasing proximity. Thus, the observed transmission minimum anomaly at intermediate weight fractions is unlikely to be due to agglomeration. Instead, we attribute this nonlinear behavior of the opacity as a coincidental photonic structure,^[30] appearing when the mean interparticle distance passes through the visible-wavelength region at intermediate weight fractions.^[31] A continued increase in particle load further decreases interparticle distances, which moves this resonance wavelength out of the discussed visible length-scale region, and the material becomes more transparent again.

As a next step, we focus our attention on the mechanical performance of printed ceramic microlattices with different densities and 3D architecture. The considered ceramic candidate structures are displayed in **Figure 3**, and the corresponding mechanical data are summarized in **Figure 4**. It is noteworthy that the original raw material and sample structures sintered up to 1450 °C exhibit the tetragonal phase in X-ray diffraction

(XRD) measurements; see also Figure S4 (Supporting Information). Solid printed cubes sintered at 800 and 1200 °C, respectively, serve as a first reference. Figure 3a shows such a sintered monolithic cube that still exhibits some remaining line features from the 2PP printing process. Micromechanical testing using a nanoindenter returns fracture forces of ≈ 790 mN (800 °C sinter temperature) and ≈ 2800 mN (1200 °C sinter temperature), as evident from Figure 4a. At 1200 °C, sintered cubes mostly resist the available force of the transducer (2.8 N) and only one solid cube failed under these maximum loading conditions. This demonstrates an increase of the fracture force by a factor of at least 3.5 with increasing sintering temperature, while a sintering temperature of 800 °C is exceptionally low for zirconia.

Resorting to more complex 3D structures, the well-known SchwarzP (SP) geometry^[32] is printed in both solid (sintered at 800 and 1200 °C) and hollow (sintered at 800, 1200, and 1450 °C) forms. The solid SP structure fills 56% of the volume compared to a cube. Figure 3c shows such a solid SP structure. Figure 3d, on the other hand, depicts a hollow SP structure. The smallest achieved ligament size of ≈ 500 nm in the x - y plane is indicated in Figure 3b. Despite the intricate geometry

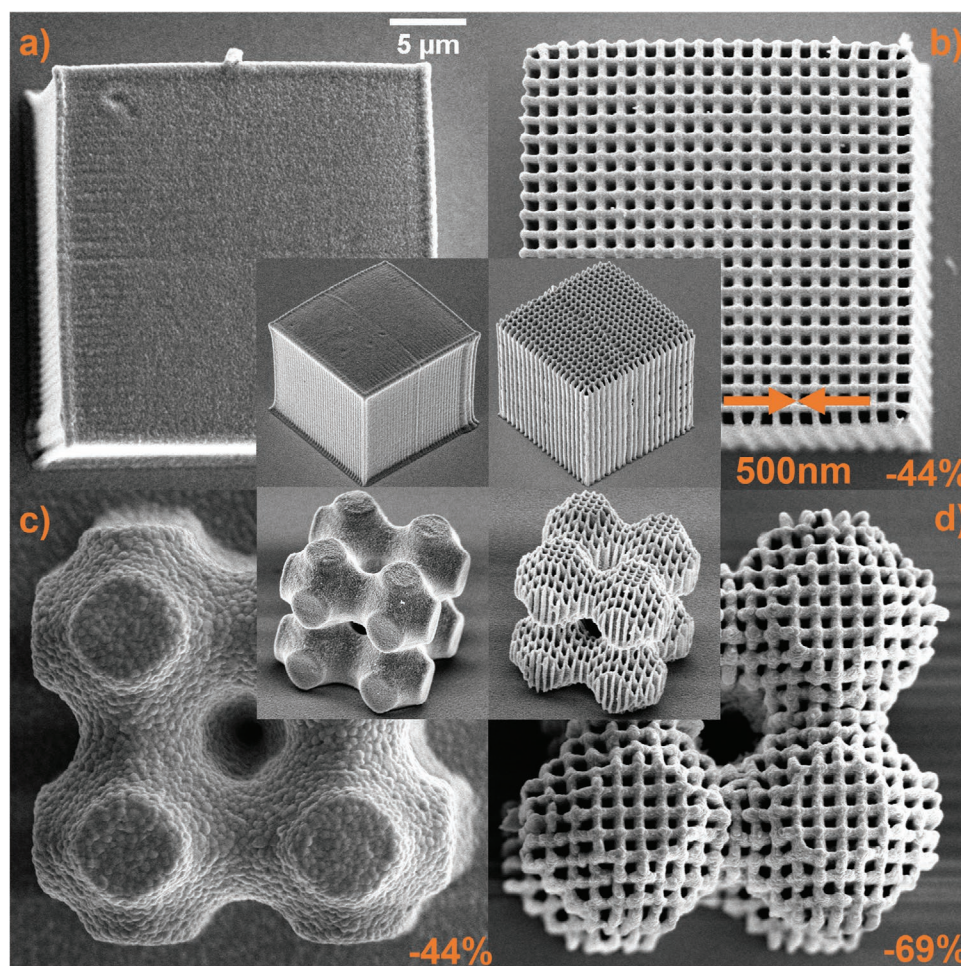


Figure 3. 2PP-printed and sintered yttria-stabilized zirconia nanostructures. a) A fully solid and b) hollow lattice cube, sintered at 1200 °C. A resolution of 500 nm is highlighted in panel (b). c,d) A solid (sintered at 1450 °C) and hollow (sintered at 1200 °C) SchwarzP structures, respectively. The density difference to the full cube in panel (a) is indicated in the lower right corner of panels (b)–(d). All pictures were taken with the same magnification.

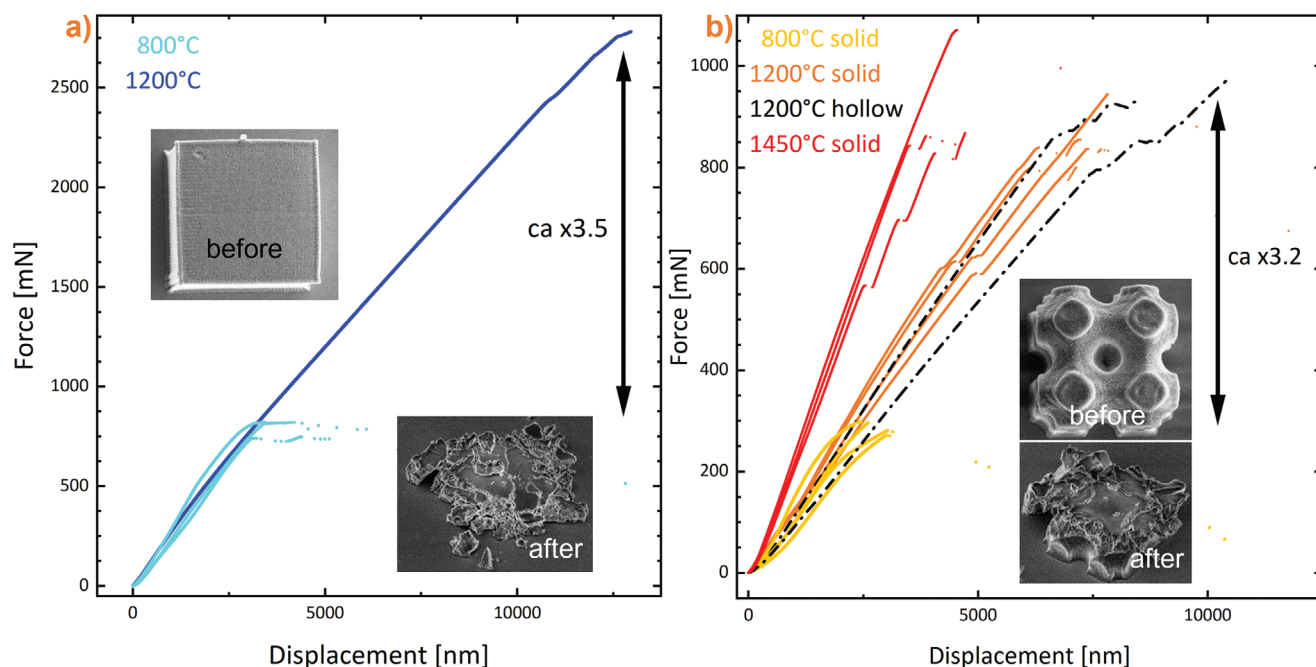


Figure 4. Micromechanical performance of 2PP-printed solid and hollow yttria-stabilized zirconia structures. a) Force–displacement curves of solid cubes sintered at both 800 and 1200 °C. Sintering at 1200 °C leads to compressive forces exceeding the limit of the sensor, equivalent to ≈ 4.5 GPa. b) Solid and hollow SchwarzP structures fracture at similar forces after sintering at or above 1200 °C, indicating strength saturation.

and the fact that a ceramic material is tested, the mechanical data shown in Figure 4b demonstrate a high reproducibility for both SP-structures. As for the cubes, a factor larger than 3 (3.2) was observed for the failure force for the hollow and the dense SP structures when increasing the sintering temperature from 800 to 1200 °C, indicating that at 800 °C sintering is just at its onset. Despite the high reproducibility of the data shown in Figure 4, the slope of the stress–strain curves should not be overinterpreted. The presented loading curves do not reflect the elastic response of the tested samples, as the supporting substrate consists of the same material at the same sintering stage, to avoid distortion during shrinkage and densification, associated to binder burn out and sintering. Required sintering temperatures for bulk zirconia often reach 1500 °C.^[33] Increasing the sintering temperature to 1450 °C yields a negligible increase in the failure force to sintering at 1200 °C; however, the slope of the respective stress–strain curves is almost doubled relative to those obtained from samples sintered at 1200 °C, indicating an increase in the modulus of elasticity of the ceramic material, that is, printed sample and supporting substrate.

Printing hollow SP microlattices reveals a designed density of the model another 43.75% lighter than the filled SP reference and 69% lighter than the solid cube (Figure 3d). Despite this significant reduction in density, the failure force stays in the range of the fully solid specimen (Figure 4b, 1200 °C). The same systematic could be observed within the cubes (Figure 3b) as the hollow cubes withstand the same maximum transducer load as their solid printed counterpart.

Instead of failure forces, it is instructive to determine the corresponding failure stress. Here we resort to dividing the normal force, as deduced from Figure 4, by the area of the structure the load is applied to. With a perfect cuboidal shape

and a larger compression tool than the examined structures, stress calculations are straight forward for solid cubes using the exact contact area. However, for complex geometries and structures with designed porosity, such as the SP and hollow structures, a different approach must be taken. For these structures, an imaginary envelope cube around the respective structure is considered. The top plane of this cuboidal envelop is used for further stress calculations, which is a very similar stress determination as used in earlier work on carbon nanolattices.^[28] In other words, when determining an equivalent fracture stress of a complex shape or hollow structure, the area over which the applied force is distributed is larger than in reality. Following this rationale, the estimated stress is representative of a given density–structure combination rather than the properties of the zirconia ceramic itself. While the chosen approach is necessary due to the intricate 3D lattice, we emphasize that this approach of stress determination significantly underestimates the true fracture stress.

A strength–density plot in Figure 5 directly compares the mechanical strength of the here-discussed ceramic structures with various material classes, and with the bulk and porous yttria-stabilized zirconia as reference materials.

Increasing the sintering temperature from 800 to 1200 °C yields a strengthening effect on all structures, which limits at 1200 °C whereas densification continues with increasing sintering temperature. This can be deduced from the SP structures summarized in Figure 5. The shift to higher densities with increasing sintering temperature eventually pushes the density of the fully solid cubes to the expected bulk density. However, sintered at 1200 °C, the solid cubes exhibit failure stresses in excess of 4 GPa since they exceed in all but one case the used sensors force range. Thus, the weakest fracture

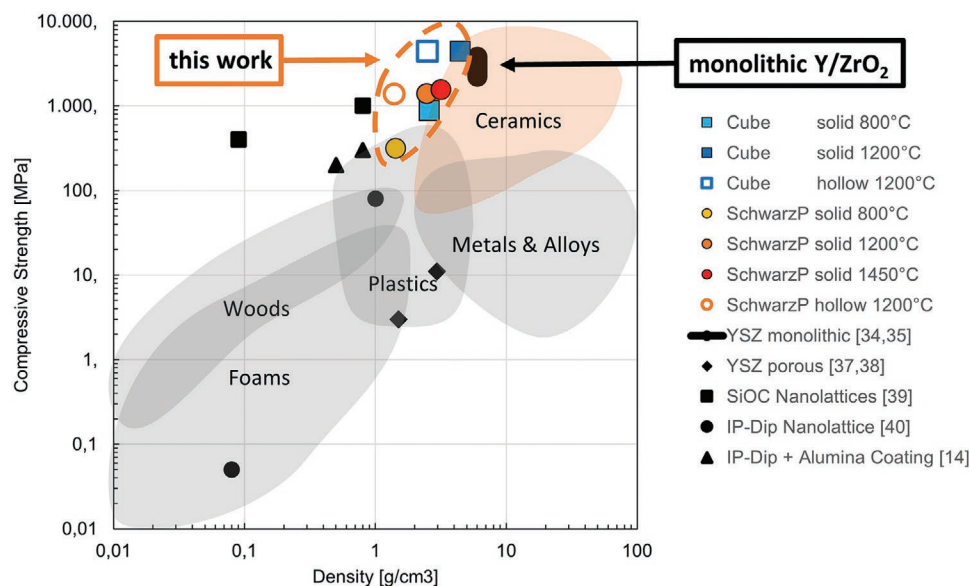


Figure 5. Strength–density correlation of various materials. Solid or hollow 2PP-written ceramic structures have significantly reduced densities but are stronger than their monolithic bulk counterparts and clearly outperform PDCs and other known porous zirconia types.

stresses of the solid 2PP-AM material is comparable to the upper end of monolithic bulk zirconia, which has a compressive strength between 2000 and 3800 MPa with a density of 6.03 g cm^{-3} (cf. Figure 5).^[34,35] This comparison between the solid cube strength and the corresponding bulk ceramic must, however, be regarded with care as the fracture stress of ceramics typically scatters by a great margin. It is for this reason that a Weibull distribution normally is used to describe the mechanical properties,^[36] for which a sufficiently large data set of the here-investigated structures currently is unavailable. Furthermore, Weibull statistics entails a volumetric scaling, naturally giving rationale for the here-observed higher strength of the dense microcubes relative to the bulk material. On the other hand, Weibull statistics with the related fracture strength sampling is applied to estimate the scatter of critical defect sizes within monolithic samples, which is not required for the present structures due to the extremely small, printed features and thus predictable defect sizes.

Inspection of the aggregated data in Figure 5 shows that a density range from $\approx 1.5 \text{ g cm}^{-3}$ to the bulk value of $\approx 6 \text{ g cm}^{-3}$ can be achieved without any noticeable loss in mechanical strength. Densitywise, here the hollow SP structure (Figure 5, orange circle) stands out with only 30% of the bulk density. This can be compared to porous zirconia derived from gel casting and sintered at temperatures as high as 1550 °C (black diamonds in Figure 5),^[37] showing compressive strengths, orders of magnitude lower (3–11 MPa^[38]) at a comparable density. Another relevant comparison is additively manufactured ceramic-like PDC either with pyrolysis into SiOC^[39] (Figure 5, black square) or without^[40] (Figure 5, black circle). Even if the addition of an alumina coating^[14] (Figure 5, black triangle) increases the compressive strength of such PDCs, values close to pure pyrolyzed SiOC Nanolattices or those of the here printed yttria-stabilized zirconia are far from being reached.

Letting aside the adapted stress determination of the complex 3D structures, the solid cubes alone demonstrate that the

presented novel 2PP-AM route generates micrometer-sized monolithic ceramics with strengths comparable or even higher than the bulk material. In the case of the complex and also hollow structures, only an underestimation of a stress equivalence can be determined, but in all cases these do not—despite the substantial density reduction—exhibit a loss in mechanical stability.

Fundamental to this advance is the formulation of a 2PP-resin bearing ceramic nanoparticles small enough to admit substantial photon transmission. The obtained structures demonstrate the creation of a pure YSZ–ceramic component that clearly demarcates from early ceramic-based efforts relying on PDCs. Demonstrated for YSZ, the described approach is expected to be applicable to most technical ceramics. It paves the way for a new family of directly 2PP-AM 3D printable lightweight structural metamaterials and artificial microstructures. They will not only inherit the chemical resistance, thermal stability, and functional properties of their bulk counterparts, but can also benefit from the design freedoms, additive manufacturing is known to offer. Extrapolation of 2PP manufacturing technologies to macroscopic printing envelopes is possible with existing technology already; see Figure S5 (Supporting Information).

3. Conclusion

The present communication demonstrates, for the first time, the possibility of applying the 2PP for the manufacture of complex-shaped advanced ceramic structures following the classical powder processing route. The effect of light scattering on the ceramic (zirconia) particles in suspension has been reduced to a negligible level by the usage of extremely well-dispersed nanoparticles. This transparent zirconia slurry with a solid load of up 80 wt% shows a high transparency and allows local crosslinking of its photocurable organics by femtosecond laser

pulses at 800 nm wavelength. Complex 3D structures have been successfully printed with a resolution of 500 nm, washed, and sintered to dense ceramic structures. Measured compressive strength values are similar to monolithic yttria-stabilized zirconia samples, but at the same time an internal structuring results in a significantly reduced density.

4. Experimental Section

Material Preparation and Characterization: The feedstock for the 2PP process is a photocurable poly-(ethylene glycol) diacrylate (PEG-DA) resin (average $M_n = 250$, Sigma-Aldrich) with 70 wt% of yttria-stabilized zirconia nanoparticles (nanoBinder, CeraNovis GmbH). For either 2PP processing or UV curing the photoinitiators 2,5-bis[4-[N,N-bis-[2-(acetyloxy) ethyl]phenyl]-methylene]-2E,5E-cyclopentanone (BAE, Genosynth) and 2,2-dimethoxy-2-phenylacetophenone (DMPA, Sigma-Aldrich) were used respectively.

Sixteen thin films were prepared of the UV-cured resin with a ceramic content ranging from 0 to 80 wt% (corresponding to a particle volume fraction of $\approx 44\%$) using a concentration series following the ISO 3 Rénard preferred number series. The films were produced with a homogeneous thickness of ≈ 0.1 mm. UV-vis transmission measurement inside cleavable quartz cuvettes (Hellma Analytics) with a thickness of 0.1 mm was performed using a StellarNet Inc. BLACKComet C-50 spectrometer with an SL5 deuterium halogen light source.

SAXS and wide-angle X-ray scattering (WAXS) measurements on these films were conducted using the Methodology Optimization for Ultrafine Structure Exploration (MOUSE) instrument, following an in-house developed, traceable methodology.^[41]

2PP Sample Preparation: To produce a base for 2PP printing, the UV-curable resin was placed inside a rectangular spacer with a few millimeters in length and up to half a millimeter in height and covered with a microscope cover slide. The resin was illuminated through the upper cover slide with an UV-LAMP for up to 20 min. On top of the so-obtained photocured foil substrate, 2PP-curable resin was placed within another spacer of 100–300 μm thickness and was covered with a 30 μm glass slide. This gave a printable volume of a few millimeters in the x-y plane and 100–300 μm in the Z-direction.

2PP Printing Setup: 3D printing was performed using a two-photon-polymerization instrument (Nanofactory, Femtika, Ltd.),^[42] employing a femtosecond laser light source (C-Fiber 780 High Power, Menlo Systems GmbH) operating at 100 fs pulse duration, 100 MHz repetition rate, and 780 nm wavelength. The laser was passed through a 60×1.4 numerical aperture immersion oil objective lens (Carl Zeiss AG). The positioning system combined linear stages ANT130XY-160 (Aerotech Inc.) for the x-y plane, ANT130LZS-060 (Aerotech Inc.), for the Z-direction, and

galvo-scanners (AGV-10HPO (Aerotech Inc.) for image projection. Programming tasks and controlling the process were done by 3DPoli software (Femtika Ltd.).

2PP Printing Process: Printing geometries and their STL-files were obtained from an open-source platform. Simple geometries like cubes were generated manually. Special geometries, like the SchwarzP triple-periodic minimal surface structure,^[43] were produced using in-house developed software^[44] based on an open-source software for the design of tissue engineering scaffolds.^[45] Transformation of the STL format into machine-readable G-Code was realized by the open-source software Ultimaker Cura (4.8.0).^[46] The CAD models were translated into G-Codes for each single structure according to **Table 1** (ordered after the structure in the Ultimaker Cura Software).

All structures were printed on top of the supporting substrate foil without additional top and bottom layers to save printing time and to give room for uncured resin to escape during washing. The chosen infill pattern was a simple grid, which was turned to match the direction of the printer single axis movement. If a wall was printed, the regime was chosen to print the wall after the infill to ensure a good connection between infill and wall. Hollow structures missed the outer walls, had a larger layer height and smaller infill density compared to solid structures. The important G-Code needs to be divided by 1000 to transform millimeter into micrometer. All structures were printed with a speed of 10.000 $\mu\text{m s}^{-1}$ and a power of 8 mW in a bottom-up way of fashion.

Printed structures were washed using ethanol (absolute water free min. = 99.5%, Sigma-Aldrich) to remove uncured material. After washing, the structures were dried via critical point drying (EM CPD300, Leica).

Thermal debinding and sintering was performed with the following temperature schedule: 0 \rightarrow 150 $^{\circ}\text{C}$ (1 K min^{-1}) \rightarrow 250 $^{\circ}\text{C}$ (0.1 K min^{-1}) \rightarrow 265 (1 K min^{-1}) \rightarrow 300 $^{\circ}\text{C}$ (0.1 K min^{-1}) \rightarrow 350 $^{\circ}\text{C}$ (1 K min^{-1}) \rightarrow 400 $^{\circ}\text{C}$ (0.1 K min^{-1}) \rightarrow 800/1200/1450 $^{\circ}\text{C}$ (1 K min^{-1} , dwell 2 h) \rightarrow 0 $^{\circ}\text{C}$ (5 K min^{-1}).

Microscopy Analysis and Mechanical Characterization: For structural characterization of printed samples, a scanning electron microscope (EVO MAT0, Carl Zeiss GmbH) was employed.

A cross-sectional cut was performed using an focused ion beam (FIB)/scanning electron microscopy (SEM) system (Quanta 3D FEG, FEI Company) equipped with a gallium source. After localizing the region of interest, a protective and smoothing platinum layer was deposited on the surface using an in situ chemical vapor deposition system. A surrounding volume material was excavated, and a fiducial structure was generated for beam alignment. Subsequently, the volume was cut using an acceleration voltage of 30 kV and a current of 30 nA, successively, decreasing to 7 nA and finally 1 nA. After cutting an SEM image was recorded.

The mechanical response of printed structures (SchwarzP and cubes) was characterized with a Hysitron T1980 equipped with a

Table 1. Ultimaker Cura parameters: generating the G-Code from CAD models in either solid or hollow printing way.

G-Code Parameters		2nd Order Parameters	3rd Order Parameters	Solid	Hollow
Quality		Layer height	[mm]	0.2	1
Shell		Wall thickness	[mm]	0.8	0.8
			Wall line count	[a.u.]	1
		Top/bottom thickness	[mm]	1	1
			Top layers	[a.u.]	0
			Bottom layers	[a.u.]	0
Infill		Infill density	[%]	80	20
			Infill line distance	[mm]	0.5
			Infill pattern	Grid	Grid
			Infill line directions	[0,90]	[0,90]
		Infill before walls	Infill first	Infill first	

high-load omniprobe transducer from Bruker using a flat punch tip of 100 μm in diameter. After precleaning the tip to remove residual debris by indentation of polycarbonate, the mechanical characterization of individual structures was performed by load-controlled indentation at a constant loading rate of 0.1 N s^{-1} to the point of fracture. Density of the nanolattices was calculated from computer-aided models, dimensions from SEM images and the known Y/ZrO_2 volume fraction from as-printed structures before sintering.

Supporting Information

Supporting Information is available from the Wiley Online Library or from the author.

Acknowledgements

The authors thank Dr. rer. nat. Frank Meyer, CEO CeraNovis GmbH, for the generous material support. Parts of this work was performed at the electron microscopy center at BAM, with special thanks to René Hesse at division 5.1. Special thanks also to Dominik Al-Sabbagh for the XRD measurements. The authors are grateful for funds provided by the Federal Institute of Materials Research and Testing (BAM).

Open access funding enabled and organized by Projekt DEAL.

Conflict of Interest

The authors declare no conflict of interest.

Data Availability Statement

Research data are not shared.

Keywords

ceramics, meta materials, powder processing, transparency, two-photon polymerization, yttria-stabilized zirconia

Received: September 20, 2022

Revised: November 14, 2022

Published online:

- [1] R. Lakes, *Nature* **1993**, 361, 511.
 [2] L. Mishnaevsky, M. Tsapatsis, *MRS Bull.* **2016**, 41, 661.
 [3] I. Giorgio, M. Spagnuolo, U. Andreus, D. Scerrato, A. M. Bersani, *Math. Mech. Solids* **2021**, 26, 1074.
 [4] L.-H. Chen, Y. Li, B.-L. Su, *Natl. Sci. Rev.* **2020**, 7, 1626.
 [5] Y. Liu, X. Zhang, *Chem. Soc. Rev.* **2011**, 40, 2494.
 [6] S. Xiao, T. Wang, T. Liu, C. Zhou, X. Jiang, J. Zhang, *J. Phys. D: Appl. Phys.* **2020**, 53, 503002.
 [7] S. Babae, J. Shim, J. C. Weaver, E. R. Chen, N. Patel, K. Bertoldi, *Adv. Mater.* **2013**, 25, 5044.
 [8] L. Mizzi, A. Spaggiari, *Smart Mater. Struct.* **2020**, 29, 105036.
 [9] M. Yin, X. Y. Tian, H. X. Han, D. C. Li, *Appl. Phys. Lett.* **2012**, 100, 124101.
 [10] J. Zeng, X. Wang, J. Sun, A. Pandey, A. N. Cartwright, N. M. Litchinitser, *Sci. Rep.* **2013**, 3, 2826.
 [11] J. Fan, L. Zhang, S. Wei, Z. Zhang, S.-K. Choi, B. Song, Y. Shi, *Mater. Today* **2021**, 50, 303.
 [12] V. F. Paz, M. Emons, K. Obata, A. Ovsianikov, S. Peterhänzel, K. Frenner, C. Reinhardt, B. Chichkov, U. Morgner, W. Osten, *J. Laser Appl.* **2012**, 24, 042004.
 [13] F. Formanek, N. Takeyasu, T. Tanaka, K. Chiyoda, A. Ishikawa, S. Kawata, *Opt. Express* **2006**, 14, 800.
 [14] J. Bauer, S. Hengsbach, I. Tesari, R. Schwaiger, O. Kraft, *Proc. Natl. Acad. Sci. USA* **2014**, 111, 2453.
 [15] L. R. Meza, J. R. Greer, *J. Mater. Sci.* **2014**, 49, 2496.
 [16] L. Brigo, J. E. M. Schmidt, A. Gandin, N. Michieli, P. Colombo, G. Brusatin, *Adv. Sci.* **2018**, 5, 1800937.
 [17] F. Kotz, A. S. Quick, P. Risch, T. Martin, T. Hoose, M. Thiel, D. Helmer, B. E. Rapp, *Adv. Mater.* **2021**, 33, 2006341.
 [18] T. A. Pham, D.-P. Kim, T.-W. Lim, S.-H. Park, D.-Y. Yang, K.-S. Lee, *Adv. Funct. Mater.* **2006**, 16, 1235.
 [19] X. Wen, B. Zhang, W. Wang, F. Ye, S. Yue, H. Guo, G. Gao, Y. Zhao, Q. Fang, C. Nguyen, X. Zhang, J. Bao, J. T. Robinson, P. M. Ajayan, J. Lou, *Nat. Mater.* **2021**, 20, 1506.
 [20] L. R. Meza, S. Das, J. R. Greer, *Science* **2014**, 345, 1322.
 [21] J. Schmidt, L. Brigo, A. Gandin, M. Schwentenwein, P. Colombo, G. Brusatin, *Addit. Manuf.* **2019**, 30, 100913.
 [22] H. Cui, R. Hensleigh, H. Chen, X. Zheng, *J. Mater. Res.* **2018**, 33, 360.
 [23] J. C. Sanger, B. R. Pauw, H. Sturm, J. Gunster, *Open Ceram.* **2020**, 4, 100040.
 [24] A. A. Griffith, G. I. Taylor, *Philos. Trans. R. Soc., A* **1921**, 221, 163.
 [25] T. Zhu, Z. Xie, *J. Am. Ceram. Soc.* **2022**, 105, 1617.
 [26] H. Gao, B. Ji, I. L. Jager, E. Arzt, P. Fratzl, *Proc. Natl. Acad. Sci. USA* **2003**, 100, 5597.
 [27] C. R. Kurkjian, *J. Non-Cryst. Solids* **1985**, 73, 265.
 [28] J. Bauer, A. Schroer, R. Schwaiger, O. Kraft, *Nat. Mater.* **2016**, 15, 438.
 [29] S. Pabisch, B. Feichtenschlager, G. Kickelbick, H. Peterlik, *Chem. Phys. Lett.* **2012**, 521, 91.
 [30] P. Vukusic, J. R. Sambles, *Nature* **2003**, 424, 852.
 [31] K. C. Wu, K. F. Seefeldt, M. J. Solomon, J. W. Halloran, *J. Appl. Phys.* **2005**, 98, 024902.
 [32] H. A. Schwarz, in *Gesammelte Mathematische Abhandlungen: Erster Band 223–269*, Springer, Berlin **1890**.
 [33] B. Stawarczyk, M. Ozcan, L. Hallmann, A. Ender, A. Mehl, C. H. F. Hammerlet, *Clin. Oral Investig.* **2013**, 17, 269.
 [34] Hochleistungskeramik Zirkonoxidkeramik CR105 und CR101, 06 <https://oxidkeramik.de/oxidkeramik-werkstoffe/zirkonoxidkeramik> (accessed: June 2022).
 [35] Zirkonoxidkeramik (ZrO₂), <https://tkc-keramik.de/werkstoffe/oxidkeramik/zirkonoxidkeramik-zro2> (accessed: June 2022).
 [36] H. Salmang, H. Scholze, R. Telle, *Keramik*, Springer, Berlin **2007**.
 [37] L. Hu, C.-A. Wang, *Ceram. Int.* **2010**, 36, 1697.
 [38] L. Hu, C.-A. Wang, Y. Huang, *J. Mater. Sci.* **2010**, 45, 3242.
 [39] P. Colombo, G. Mera, R. Riedel, G. D. Sorar, *J. Am. Ceram. Soc.* **2010**, 93, 1805.
 [40] J. S. Oakdale, J. Ye, W. L. Smith, J. Biener, *Opt. Express* **2016**, 24, 27077.
 [41] G. J. Smales, B. R. Pauw, *J. Instrum.* **2021**, 16, P06034.
 [42] L. Jonuauskas, T. Baravykas, D. Andrije, T. Gadiauskas, V. Purlys, *Sci. Rep.* **2019**, 9, 17533.
 [43] P. J. F. Gandy, J. Klinowski, *Chem. Phys. Lett.* **2000**, 322, 579.
 [44] S. Fritzsche, <https://github.com/BAMresearch/ScaffoldStructures> (accessed: March 2022).
 [45] J. C. Dinis, T. F. Morais, P. H. J. Amorim, R. B. Ruben, H. A. Almeida, P. N. InforAti, P. J. Bartolo, J. V. L. Silva, *Procedia Technol.* **2014**, 16, 1542.
 [46] Ultimaker Cura Software, <https://ultimaker.com/de/software/ultimaker-cura> (accessed: January, 2022).